

See discussions, stats, and author profiles for this publication at: <https://www.researchgate.net/publication/227563089>

Unraveling Deterministic Mesoscopic Polarization Switching Mechanisms: Spatially Resolved Studies of a Tilt Grain Boundary in Bismuth Ferrite

ARTICLE *in* ADVANCED FUNCTIONAL MATERIALS · JULY 2009

Impact Factor: 11.81 · DOI: 10.1002/adfm.200900100

CITATIONS

27

READS

11

10 AUTHORS, INCLUDING:



Katyayani Seal

Oak Ridge National Laboratory

41 PUBLICATIONS 369 CITATIONS

SEE PROFILE



Arthur P Baddorf

Oak Ridge National Laboratory

170 PUBLICATIONS 3,316 CITATIONS

SEE PROFILE



Long-Qing Chen

Pennsylvania State University

222 PUBLICATIONS 4,614 CITATIONS

SEE PROFILE



Sergei V Kalinin

Oak Ridge National Laboratory

621 PUBLICATIONS 10,847 CITATIONS

SEE PROFILE

Unraveling Deterministic Mesoscopic Polarization Switching Mechanisms: Spatially Resolved Studies of a Tilt Grain Boundary in Bismuth Ferrite

By Brian J. Rodriguez,* Samrat Choudhury, Y. H. Chu, Abhishek Bhattacharyya, Stephen Jesse, Katyayani Seal, Arthur P. Baddorf, R. Ramesh, Long-Qing Chen, and Sergei V. Kalinin*

The deterministic mesoscopic mechanism of ferroelectric domain nucleation is probed at a single atomically-defined model defect: an artificially fabricated bicrystal grain boundary (GB) in an epitaxial bismuth ferrite film. Switching spectroscopy piezoresponse force microscopy (SS-PFM) is used to map the variation of local hysteresis loops at the GB and in its immediate vicinity. It is found that the influence of the GB on nucleation results in a slight shift of the negative nucleation bias to larger voltages. The mesoscopic mechanisms of domain nucleation in the bulk and at the GB are studied in detail using phase-field modeling, elucidating the complex mechanisms governed by the interplay between ferroelectric and ferroelastic wall energies, depolarization fields, and interface charge. The combination of phase-field modeling and SS-PFM allows quantitative analysis of the mesoscopic mechanisms for polarization switching, and hence suggests a route for unraveling the mechanisms of polarization switching at a single defect level and ultimately optimizing materials properties through microstructure engineering.

devices.^[4,5] The functionality of many of these systems is directly underpinned by polarization reversal processes. At the same time, all experimentally available materials are characterized by the presence of structural defects such as grain boundaries (GBs) in polycrystalline films and bulk ceramics, misfit and threading dislocations in epitaxial films, or point defects such as oxygen vacancies and vacancy dipoles and clusters inevitable in single crystalline materials. Thus, the tremendous interest in polarization switching, hysteresis, and relaxation phenomena in ferroelectric materials in the presence of extended and point-like structural defects can be easily understood.

In ferroelectric materials, defects act as pinning sites for domain wall motion and nucleation sites for polarization reversal.

Thermodynamic modeling has demon-

strated that dislocations, the predominant defect type in epitaxial ferroelectrics, locally destabilize the ferroelectric phase and account for non-switchable layers and reduced dielectric properties.^[6–9] In particular, misfit dislocations serve as effective pinning centers, as studied theoretically by Emelyanov and Pertsev^[10] and experimentally by Chu et al.^[11] In epitaxial thin

1. Introduction

The presence of switchable polarization in ferroelectric thin films enables their applications in random access memories and data storage,^[1–3] as well as a broad plethora of electromechanical sensors, actuators, RF electronic, and energy harvesting

[*] Dr. B. J. Rodriguez
Conway Institute of Biomolecular and Biomedical Research,
University College Dublin
Belfield, Dublin 4 (Republic of Ireland)
E-mail: brian.rodriguez@ucd.ie
Dr. S. V. Kalinin, Dr. S. Jesse, Dr. K. Seal, Dr. A. P. Baddorf
Center for Nanophase Materials Sciences
Oak Ridge National Laboratory
Oak Ridge, TN 37831 (USA)
E-mail: sergei2@ornl.gov
Dr. S. Choudhury, Prof. L.-Q. Chen
Department of Materials Science and Engineering
Pennsylvania State University
University Park, PA 16802 (USA)

Prof. Y. H. Chu
Department of Materials Science and Engineering
National Chiao Tung University
Hsinchu, Taiwan 30013 (ROC)

Dr. A. Bhattacharyya
Department of Materials Science and Engineering
Lehigh University
5 East Packer Avenue, Bethlehem, PA 18015 (USA)

Prof. R. Ramesh
Department of Materials Science and Engineering
University of California
Berkeley, CA 94720 (USA)

DOI: 10.1002/adfm.200900100

films, defect structures such as threading and misfit dislocations are well understood, and the density can be controlled through proper deposition conditions.^[12] However, to date, the experimental studies relating defect structures to pinning and nucleation have invariably been limited by the fact that i) the collective effect of multiple defects of different types on averaged system responses was probed and ii) the defect identity was unknown. Recent electron microscopy studies of defect-lattice interactions,^[13–15] have allowed direct observation of atomic positions and reconstruction of local polarization and its evolution in the vicinity of the defect. However, the relationship between polarization switching mechanisms and local atomic structure, i.e., deterministic switching mechanisms at a single defect level, are still elusive.

Recently, spectroscopic switching piezoresponse force microscopy (SS-PFM) has allowed switching properties, including nucleation, to be mapped at the nanoscale.^[16] Unambiguous visualization of nucleation centers and their energetic parameters, and mapping of switching behavior on a single defect level have also been demonstrated.^[17–19] However, the atomic structure and the nature of these defects are not known, precluding the elucidation of relevant mesoscopic and atomistic mechanisms. Understanding the role of defects in local ferroelectric phase stability, domain nucleation, and wall pinning requires the switching behavior to be probed at the level of a *single* defect with *known* structure. Here, we explore the feasibility of using a bicrystal GB as a model system in which defects can be visualized and ferroelectric switching properties can be measured directly.

2. Polarization Dynamics at a Bicrystal GB

The polarization switching at a single defect level is studied using spatially resolved spectroscopic imaging (SS-PFM). As a model system, we use an epitaxial BiFeO₃ (BFO) film with an engineered bicrystal GB defect. Similar BFO films exhibit single domain switching near the intrinsic thermodynamic limit^[16] and high surface stability that allows the application of multiple switching cycles with minimal surface degradation. A bicrystal GB was chosen for this study because i) the location of the defect can be determined directly by atomic force microscopy (AFM), ii) the average structure of simple GBs in cubic perovskites is generally known,^[20] and iii) a known defect structure allows for the development of mesoscopic phase-field models, thus allowing the deterministic mesoscopic polarization switching mechanisms to be determined.

A schematic of the BFO GB structure is shown in Figure 1a. The atomic and electronic structure of a prototypical GB in SrTiO₃ is well known, and is formed by the dislocation cores perpendicular to the crystal plane. Typically, the GBs in crystallographically similar compounds (e.g., SrTiO₃) have negative charge due to oxygen non-stoichiometry.^[21] While no information is available on the structure of the GB in a BFO film (the attempts for electron microscopy studies were unsuccessful due to the low mechanical stability of the bicrystal sample), the epitaxial growth of BFO on SrTiO₃ and the similarity between the crystallographic structures of the substrate and the film compounds suggest the structure of the GB can be expected to be similar.

Recently, using PFM and conducting AFM, we reported that the increased conductivity at the GB is a possible domain pinning

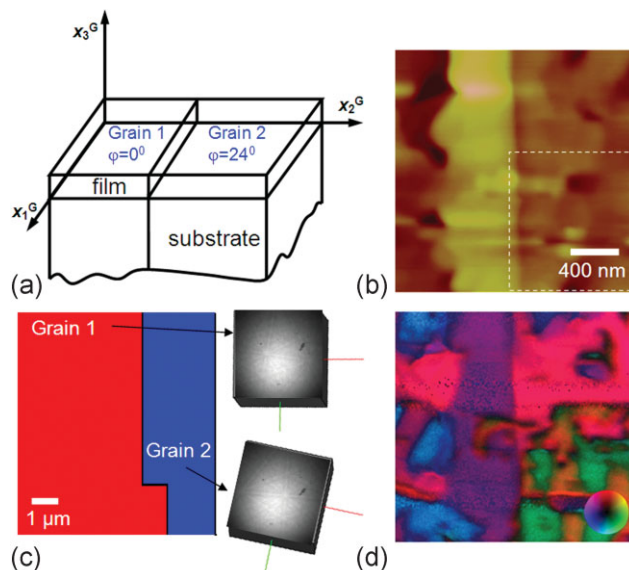


Figure 1. a) Schematic diagram of the BFO bicrystal (grain 2 rotated 24° about x_3), b) topography, c) EBSD with diffractograms, and d) vector PFM image. The lower right corner had been switched prior to obtaining this image, as indicated with the dashed line in (b). The hue and intensity of the color provides information on the polarization orientation and magnitude, respectively, as illustrated by color wheel in (d). The typical as-grown domain structure is shown in the Supporting Information.

mechanism.^[22] Here, we use PFM and SS-PFM to examine the switching properties, specifically the nucleation mechanism, in detail. In addition, electron backscatter diffraction (EBSD) is used to probe the structure/orientation at the junction. Finally, the experimental results are compared with a phase-field model to establish the mesoscopic switching mechanism in an ideal film and near a GB.

2.1. Domain Structure at the GB

The topographic structure of the BFO GB region is shown in Figure 1b. On the substrate, sample preparation (etching and annealing) typically results in a groove located at the GB (not shown). After the SrRuO₃ (bottom electrode) and BFO growth, the GB is associated with a clear topographic feature extending ~400–500 nm from the GB. The ridge is non-uniform along the length of the GB and could be on either (or both) side(s) of the GB.^[23] Despite the presence of the ridge, the film roughness is less than 2 nm. To verify the ridge is not associated with deviations in crystallographic structure or primary crystallographic orientation, the bicrystal surface was mapped by EBSD. The EBSD results verify the 24° mismatch between the substrate crystals (Fig. 1c) and indicate the absence of stray phases in the vicinity of the GB.

The domain structure for a partially switched region is shown in the vector PFM^[24] image in Figure 1d. The hue and intensity of the color provide information on the polarization orientation and magnitude, respectively, as illustrated by the color wheel. The in- and out-of-plane PFM amplitude and phase images are shown in

the Supporting Information. The 2D vector PFM image allows the domain structure at the GB to be visualized. As anticipated, the domain pattern and possible orientations change at the interface (as stipulated by crystallographic structure).

In Ref. [22], the GB was found to act as a pinning center for a moving domain wall, and the behavior was correlated with increased conductivity at the GB. Despite similarities between the surface topography on the GB edge and the overgrowth edge, the static polarization behavior is significantly different, suggesting that the effect of the GB can be studied notwithstanding the noticeable contribution to the observed PFM contrast from topographic cross-talk. The high-resolution topography and domain structure (PFM amplitude and phase) images of another location are shown in Figure 2a–c. A careful examination of the PFM amplitude data and domain morphology reveals that the GB can be associated with three characteristic domain-behaviors as determined from vertical (out-of-plane) PFM (and indicated by numbered circles in Figure 2b):

- (1) There is a reduction in amplitude across the GB if the surrounding matrix is polarized negatively. The width of this region is similar to the measured domain wall width (i.e., the

width is likely determined by PFM resolution, rather than the intrinsic GB width).

- (2) There is no reduction in piezoresponse when the surrounding matrix is positively polarized.
- (3) When each side is polarized in the opposite direction, the GB acts as a pinning site, i.e., the domain wall coincides with the GB.

These observations provide the information about *static* domain structures (i.e., thermodynamic equilibrium) at the GB, and domain wall *pinning* mechanisms. Below, we specifically study the domain *nucleation* at the GB and at the ideal surface.

2.2. Switching Spectroscopy PFM of the GB

To investigate the ferroelectric switching and domain nucleation mechanism spatially across the GB interface, SS-PFM was employed. In these measurements, an array of 60×60 local electromechanical hysteresis loops is acquired over a square spatial grid with 15 nm pixel spacing. The resulting 3D data array is analyzed to yield 2D maps of the effective work of switching (area within the loop), positive and negative nucleation biases, and other relevant switching parameters.^[25,26] These maps allow the dynamic polarization behavior to be directly correlated with the local microstructure and the GB and topography induced changes in polarization switching to be differentiated. After the SS-PFM mapping, the area can be scanned in the PFM mode to directly visualize the region in which measurements were taken (and hence compensate for microscope drift inevitable during long 2–6 h scans).

The SS-PFM maps of positive and negative nucleation bias are shown in Figure 2d and e, respectively. Note that the positive nucleation bias is reduced at the GB, while the absolute value of the negative nucleation bias increases at the GB, suggesting the GB accelerates nucleation with a positive bias and delays nucleation with a negative bias. Similarly, the positive nucleation biases are roughly equivalent on either side of the GB, while a larger negative bias is required to switch the film on the right side of the GB. The complete set of SS-PFM images is available in the Supporting Information. In general, the film is negatively imprinted; however, this imprint becomes more pronounced at the GB, consistent with the change in nucleation biases and our previous report on domains adhering to the GB.^[22] Line profiles of switching properties are illustrated in Figure 2f and g. Most parameters of switching properties including switchable polarization, work of switching, and piezo-response are strongly affected by the presence of the GB, resulting in a characteristic N-type

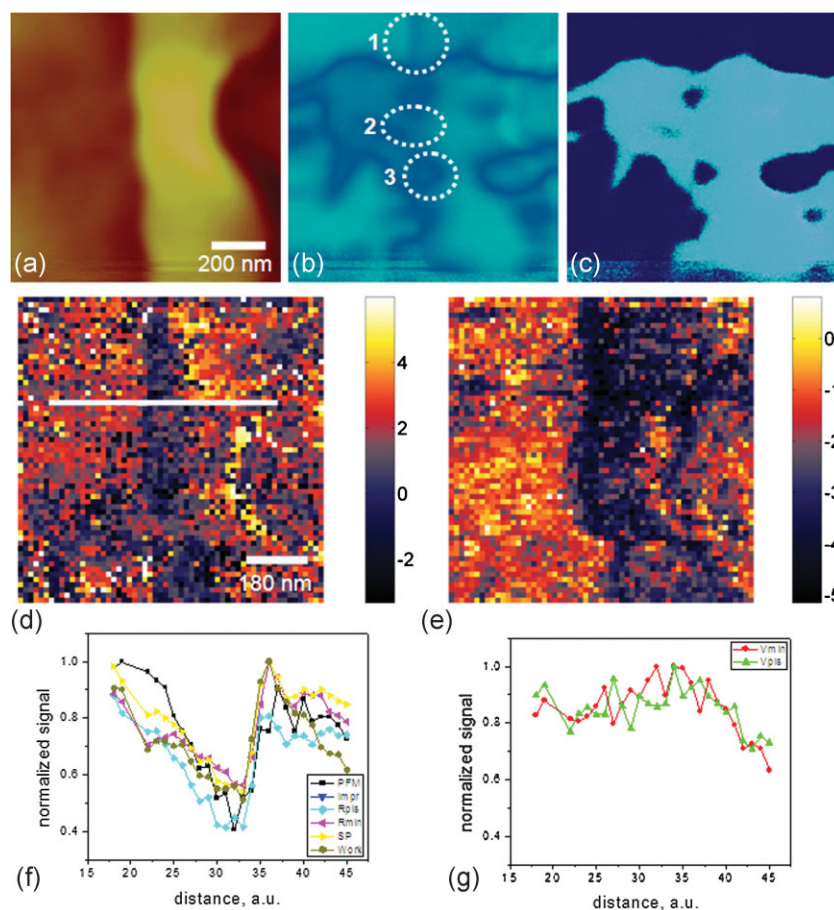


Figure 2. a) Topography, b) PFM amplitude, and c) PFM phase images. d,e) 2D SS-PFM maps of positive and negative nucleation bias, respectively. The SS-PFM maps have 60×60 data points with a 15 nm pitch. f,g) Line profiles of switching properties across the GB from the location indicated with a white line in (d). The GB does not appear straight due to microscope drift.

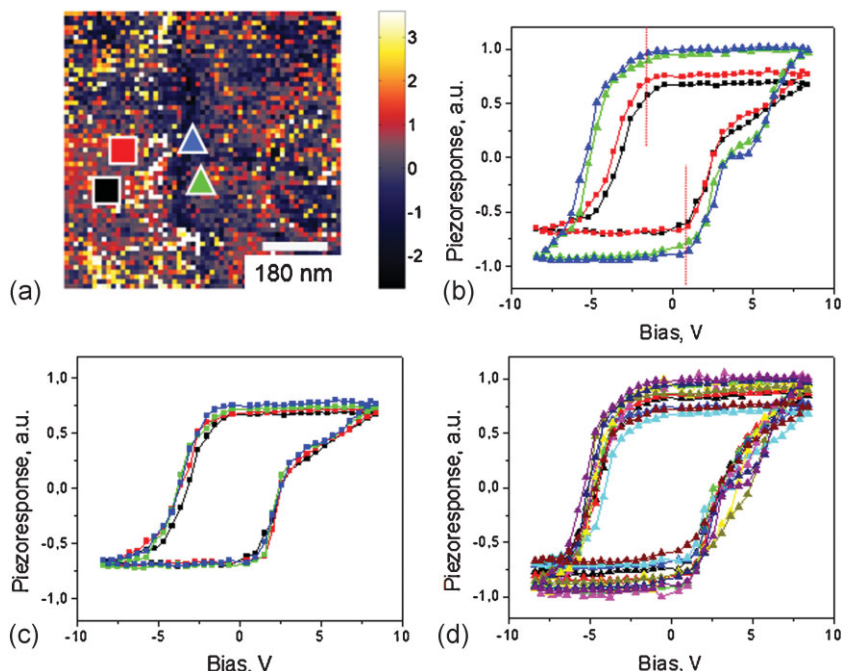


Figure 3. a) 2D SS-PFM map of imprint. b) Representative hysteresis loops from the film and near the GB, from roughly the locations marked in (a). c, d) Hysteresis loops from the film (c) and near the GB (d). Red lines in (b) are drawn as a guide to the eye to delineate differences between ideal loops and those affected by the GB.

profile. At the same time, coercive biases are almost unaffected by the GB, illustrating that in the strong field of a PFM probe, the GB-effect on pinning is relatively small (pinning becomes significant at much larger domain sizes). Hysteresis loops (Fig. 3b–d) extracted from the film and close to the GB clearly demonstrate the difference in negative nucleation bias and increased imprint (Fig. 3a). Near the GB, the loop becomes wider and the switchable piezoresponse larger, corresponding to an increased work of switching and coercive field. At the same time, the imprint increases while the switchable piezoresponse remains symmetric.

The comparison of the hysteresis loops from the vicinity of the GB and the rest of the surface illustrate several interesting features about the loop shapes. Loops from the GB region (green and blue loops in Fig. 3b) exhibit delayed nucleation in one direction and a fine structure feature in other. At the same time, the loops measured away from the GB (red and black loops) are ideal. The nucleation on the reverse branch matches the second (apparent) nucleation on the forward branch (at ~ 5 V). Furthermore, the nucleation is delayed on the reverse branch compared to the forward branch. The linear slope of the forward branch from ~ 3 V (i.e., the late switching stage) is about three times higher close to the GB, suggesting that while the initial growth is the same, the domain grows faster when it interacts with the GB. Similarly, the topographic features are associated with variations in measured switching behavior (the edge of the overgrowth region serves as an internal comparison). However, the changes in the switching behavior induced by the presence of the GB can be clearly differentiated from the background.

3. Mesoscopic Mechanisms of Polarization Switching at the GB

The effect of the GB on polarization switching and nucleation can be complex due to the combination of mesoscopic and atomistic effects. The mesoscopic effects include i) intrinsic mismatch between crystallographic orientations, ii) long-range strain and electrostatic fields related to the polarization discontinuity at the GB, and iii) strains produced by dislocation cores. Additionally, the defect and vacancy segregation at the interface can produce additional interface charge, resulting in long-range space charge layers in the vicinity of the GB. Finally, GB conductivity and changes in the screening length in the vicinity of the GB can significantly affect the structure of electrostatic field produced by the AFM tip, modifying the probing volume.

Clearly, the atomistic effects of a GB can be addressed only once the electronic structure of the interface and the interface charge are known. However, these fields can be expected to be significant on the length scale of the depletion region or Debye length of the material. The intrinsic conductivity of the interface^[22] suggests electrostatic screening will be limited to extremely short (below 10 nm) distances in the vicinity of the domain

wall. Due to the presence of the divot on the sample surface, this will result in either a highly localized feature in the SS-PFM image (the total width cannot be larger than the width of the GB region and the characteristic size of the nucleating domain), or be unobservable due to the fact that the tip apex cannot contact the bottom of the divot. At the same time, mesoscopic effects related to the elastic strain field and associated piezoelectric-induced electrostatic fields will be active on the length scale of the film thickness (~ 20 – 50% of the film thickness^[27]), and hence are likely associated with contrast visible on much larger length scales.

3.1. Phase-Field Modeling of Switching Near a GB

The mesoscopic polarization behavior in the vicinity of a GB is studied using the phase-field method.^[16,17] For convenience, we introduced two coordinate systems, namely the global and the local coordinate system. The domain structure is described by the inhomogeneous distribution of local polarization P_i^L , where P_1^L, P_2^L, P_3^L are the polarization components in the local crystallographic coordinate system within a grain. For a bicrystal, it is necessary to describe the spontaneous strains in both the grains using a common reference coordinate system, which we refer to as the global coordinate system. The orientation of each grain is specified by a rotational angle, φ . A transformation matrix determines the relationship between the tensor components of properties in the global coordinate system denoted by a

superscript G and those in the local coordinate system within each grain. A brief description of the phase-field approach is given in the Experimental Section. Details of the phase-field approach and the material constants used in simulations can be found elsewhere.^[28–30]

A domain structure of an (001)-oriented BiFeO₃ film under a compressive substrate strain of 1% was first generated by performing the simulations under short circuit boundary conditions (Fig. 4a) starting from an initially paraelectric state with small random perturbations. The polarization distribution in the resulting system is illustrated in Figure 4 in the laboratory coordinate system. The domain structure is formed by a complex pattern of interpenetrating domains belonging to $[i,j,n]$ family, where $i, j, n = \pm 1$, separated by ferroelectric (180°) and ferroelastic (71°, 109°) domain walls. Due to crystallographic mismatch between the grains, the GB is associated with a partial ferroelastic wall and is visible as a variation of contrast in the polarization image in the global presentation, P_i^G . However, the domain generally penetrates the GB region and the GB is generally invisible in the polarization image in the crystal coordinate system, P_i^L .

The electric field and strain energy distribution in the top layer of the crystal are illustrated in Figure 4b and c. Remarkably, only the domain walls associated with the change of the normal polarization component, i.e., separating $[i,j,1]$ type domains from $[n,k,-1]$ domains, when $i, j, n, k = \pm 1$, are associated with significant electrostatic fields and strain energy. Note that the

electroelastic fields at the GB are significantly smaller than at these up-down walls.

The cross-section images in Figure 4e and h illustrate that electrostatic fields within the material have complex long-range structure, i.e., stem from depolarization fields due to polarization charges at the interfaces. Note that while domain walls are charge-neutral in the infinite stress-free material, the thermodynamic equilibrium of the finite slab results in finite wall charges as the wall geometry deviates from ideal to compensate misfit and ferroelastic stresses. The GB is associated with a strong in-plane field due to the polarization bound charge in the center of the slab, and positive and negative normal fields on the surface and interface, respectively (Fig. 4g and h). At the same time, there is only insignificant (compared to up-down walls) variation of the elastic energy density (Fig. 4i).

3.2. Mesoscopic Switching Mechanism Away from the Interface

The evolution of the polarization distribution and electric fields during polarization switching on a free surface away from the GB is illustrated in Figure 5. The electrical potential generated from the PFM tip is approximated by a Lorentz-like distribution.^[16,17] In order to find the critical nucleation potential, we gradually increase the potential in a step of 0.05 V, and the domain structure

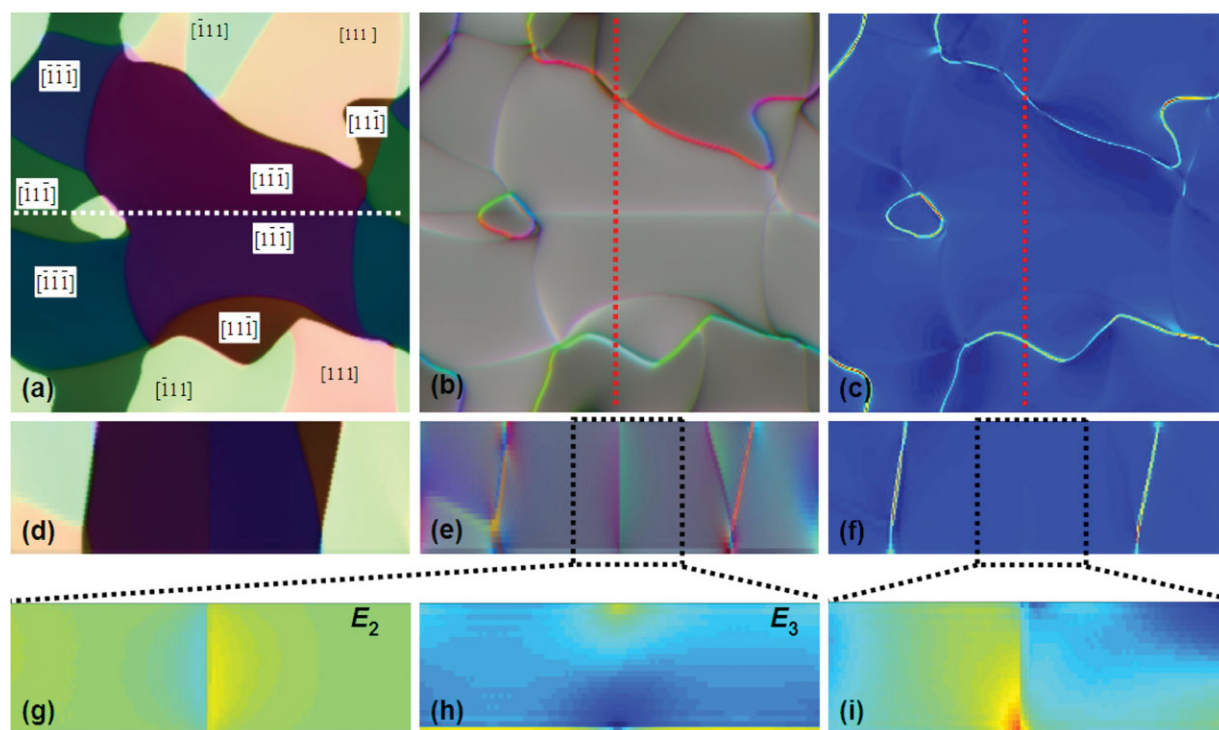


Figure 4. Domain structure and field distributions within modeled BiFeO₃ bicrystal. Shown are a,d) polarization distribution, b,e) electric field, and c,f) elastic energy. (a,b,c) correspond to the top surface, and (d,e,f) to the profile across the red lines in (b,c) correspondingly. The GB location is marked by a white dotted line in (a). The bottom crystal is aligned in (10) orientation, while the top is rotated by 24°. Also shown are g) E_2 and h) E_3 fields, and i) elastic energy in the vicinity of the GB. The characteristic field structure due to GB polarization charge and surface and interface screening is clearly seen.

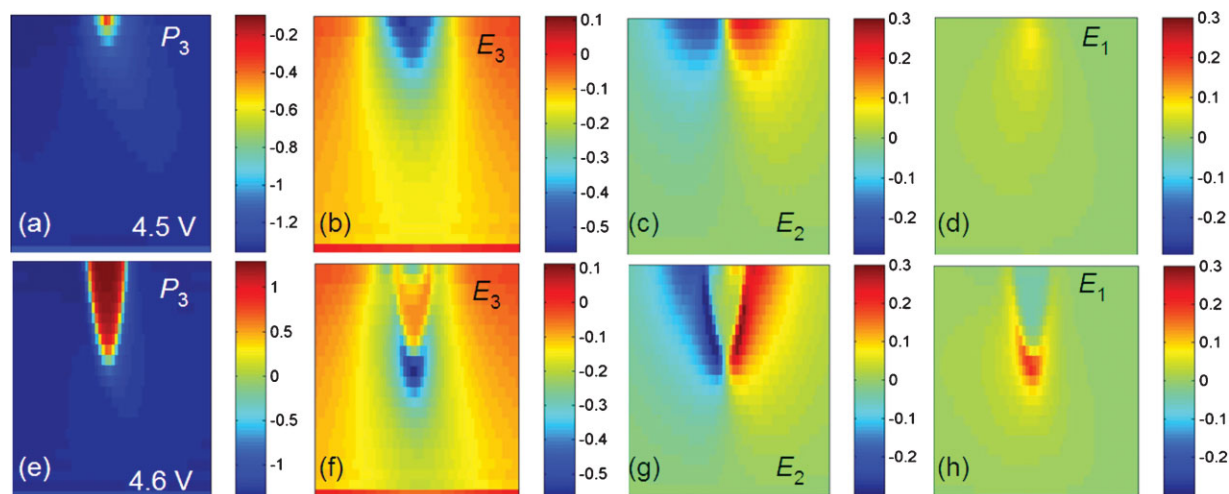


Figure 5. Evolution of domain structure and internal fields a–d) before and e–h) after nucleation. Shown are a,e) vertical polarization component, b,f) vertical electric field, c,g) field in the image plane, and d,h) electric field perpendicular to the image plane.

from a previous simulation is used as the input at each increment of the potential. At a critical applied electric potential a new rhombohedral domain is found to nucleate below the tip, and the corresponding electric potential is identified as the nucleation potential.

In the subcritical regime (below domain nucleation threshold), the polarization (Fig. 5a) below the tip deviates from the bulk value due to tip field; however, the magnitude is small compared to the absolute value. The normal component of the electric field (Fig. 5b) is concentrated below the tip, while the E_2 component (Fig. 5c) shows positive and negative lobes, as anticipated from simple electrostatic considerations. Note that the E_1 component (Fig. 5d) that would be expected to be zero in a tetragonal material from symmetry considerations has a non-zero distribution, as discussed below. The fields on the surface are illustrated in Figure 6a and c. Note that due to the rhombohedral symmetry of the material, the orientation of the in-plane polarization response maximum significantly deviates from that of the in-plane E_2 field component.

Above the nucleation threshold, a well-defined domain of opposite polarization forms (Fig. 5e). Note that switching is associated only with the reversal of the vertical polarization component, i.e., corresponds to 71° ferroelastic switching. While associated with the formation of high-energy ferroelastic walls (see Supporting Information), the formation of needle-like domains minimizes the depolarization energy. In comparison, ferroelectric 180° switching would result in an extremely unfavorable in-plane elongated nucleus. The normal field component, E_3 (Fig. 5f), now shows characteristic positive and negative regions reflecting the

depolarization field induced by the bound charges of the tip apex. Similar changes are observed on the E_2 component (Fig. 5g), which now penetrates into the material and is no longer concentrated below the tip.

Perhaps the most striking result is the observation that the domain is almost circular in cross-section (see also Fig. 6), despite the fact that the material is rhombohedral. This observation verifies the applicability of reduced models in which only changes in the normal polarization component are analyzed.

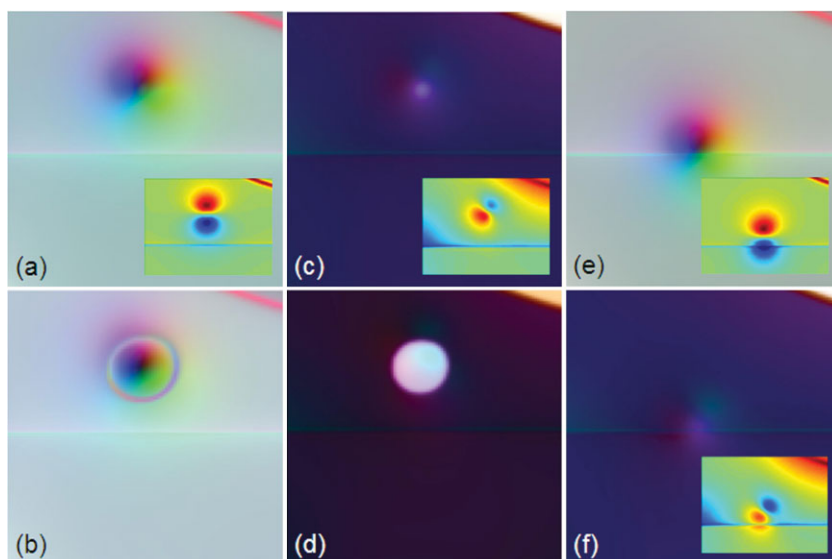


Figure 6. Field-induced polarization distribution and GB effect on switching. Shown are electric field a,b,e) and polarization c,d,f) images before (a,c,e,f) and after (b,d) switching. The simulations are performed away (a–d) and at (e,f) the GB. The insets show the distribution of the second component of the respective field (E_2 and P_2). Note that below the nucleation voltage the polarization and electric field distributions are only weakly affected by the GB. Also note the difference between the in-plane orientations of electric fields and induced polarization.

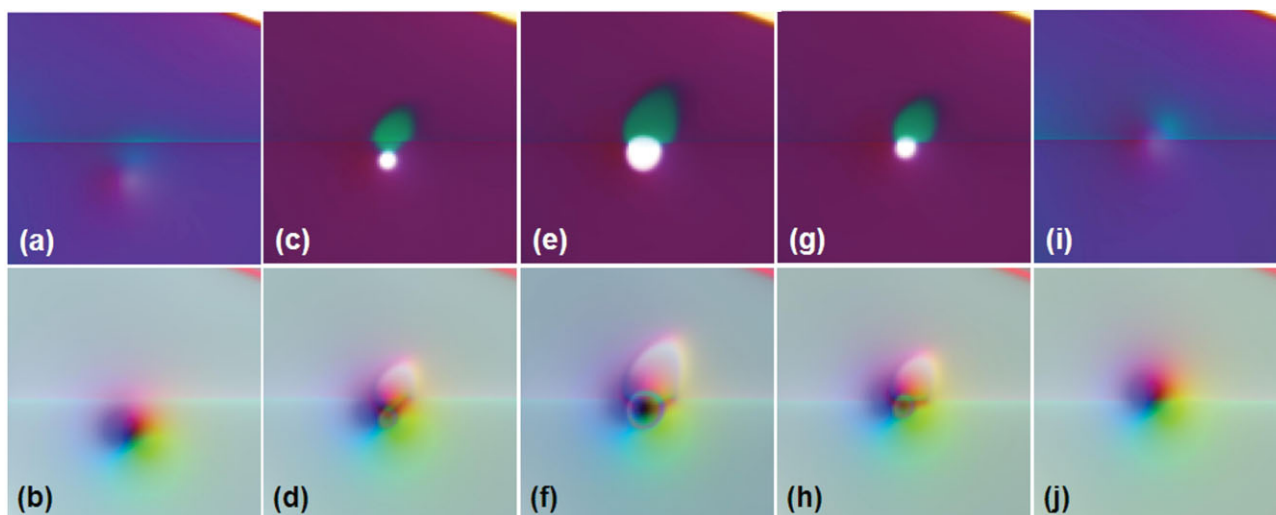


Figure 7. Variability of switching behavior across the interface. Shown are polarization (top row) and electric field (bottom row) induced by the tip at 4.5 V bias. The data are shown for locations a,b) 114, c,d) 121, e,f) 124, g,h) 126, and i,j) 128, where the GB corresponds to position 128.

3.3. Mesoscopic Mechanism of Polarization Switching at the Interface

To gain insight into the GB-mediated switching mechanism, the switching was performed in the GB region. The evolution of electroelastic fields at the surface is illustrated in Figure 6e and f (subcritical regime) and Figure 7 (above the nucleation threshold at a fixed potential). The results indicate that the presence of the GB breaks the symmetry of the nucleating domain, and results in in-plane polarization switching and the formation of a compound ferroelectric–ferroelastic domain pair.

To explore the GB-effect on polarization switching, the tip at a subcritical bias (4.5 V, as compared to onset of bulk nucleation at 4.6 V) is scanned across the GB. Spatial variability of switching behavior is shown in Figure 7, illustrating the evolution of the polarization and electric fields for different tip positions. The sequence of images (Fig. 7a–j) illustrates a remarkable change in the domain morphology. Away from the GB, the domain is not nucleated at 4.5 V. At higher voltages (Fig. 6b and d) switching is purely 71° and the resulting domain has a circular cross-section. On approaching the GB, we observe the formation of the ferroelectric–ferroelastic domain pair (Fig. 7c), noting that the ferroelastic domain (white) forms within the single crystal region 1, while the ferroelectric domain (green) forms at region 2, expands towards the GB and then shrinks and terminates at the ferroelastic domain. Further approaching the GB, the size of the ferroelectric domain grows and the junction of the ferroelectric and ferroelastically switched region is now directly at the GB. At even smaller separations (but still without crossing the GB), the GB now hinders domain nucleation. Finally, with the tip at the GB and crossing into region 2, no domain nucleation is observed.

The results of our phase-field modeling suggest that i) anomalous switching at the GB is due to the formation of a ferroelectric–ferroelastic wall pair, ii) the process is asymmetric with respect to the GB (it happens only in region 1 and not 2), and iii) the maximum reduction of nucleation bias is observed at

intermediate tip-GB separations when the maximum of the in-plane tip field, E_2 , is at the GB and the maximum of the normal field, E_3 , is in the bulk of the grain.

The bulk distribution of the corresponding energy and field components is shown in Figure 8a–f. In agreement with the above results, the ferroelastic switching results in the formation of high elastic energy density up-down walls, while ferroelectric switching results in low energy domains walls.

4. Discussion

Based on the results of mesoscopic modeling, the following mechanism of the GB-mediated polarization switching emerges. In the bulk material, tip-induced switching is purely 71° (only the normal polarization component switches) and results in the formation of a semiellipsoidal domain with high elastic energy density up-down walls. The domain is associated with an in-plane dipole as the result of mismatch between the domain axis and the polarization orientation within the material. The in-plane components of the probe field do not result in in-plane switching due to a prohibitively large depolarization field.

In the vicinity of the GB, the presence of the GB breaks the symmetry between in-plane states and the GB charge allows an effective way to screen the bulk polarization charge due to in-plane switching. The process is further facilitated by the low elastic energy of the resulting ferroelectric walls. The interplay between optimal conditions for 71° switching (maximal normal field below the tip) and ferroelectric switching (maximum in-plane field at some distance from tip-surface junction) results in the scenario when the nucleation is maximally facilitated when the tip is at a finite separation from the GB, and results in the formation of a ferroelectric–ferroelastic domain.

The spatial distribution of the nucleation potential perpendicular to the GB is plotted in Figure 8g. The figure shows that the electric potential required to nucleate a new domain increases

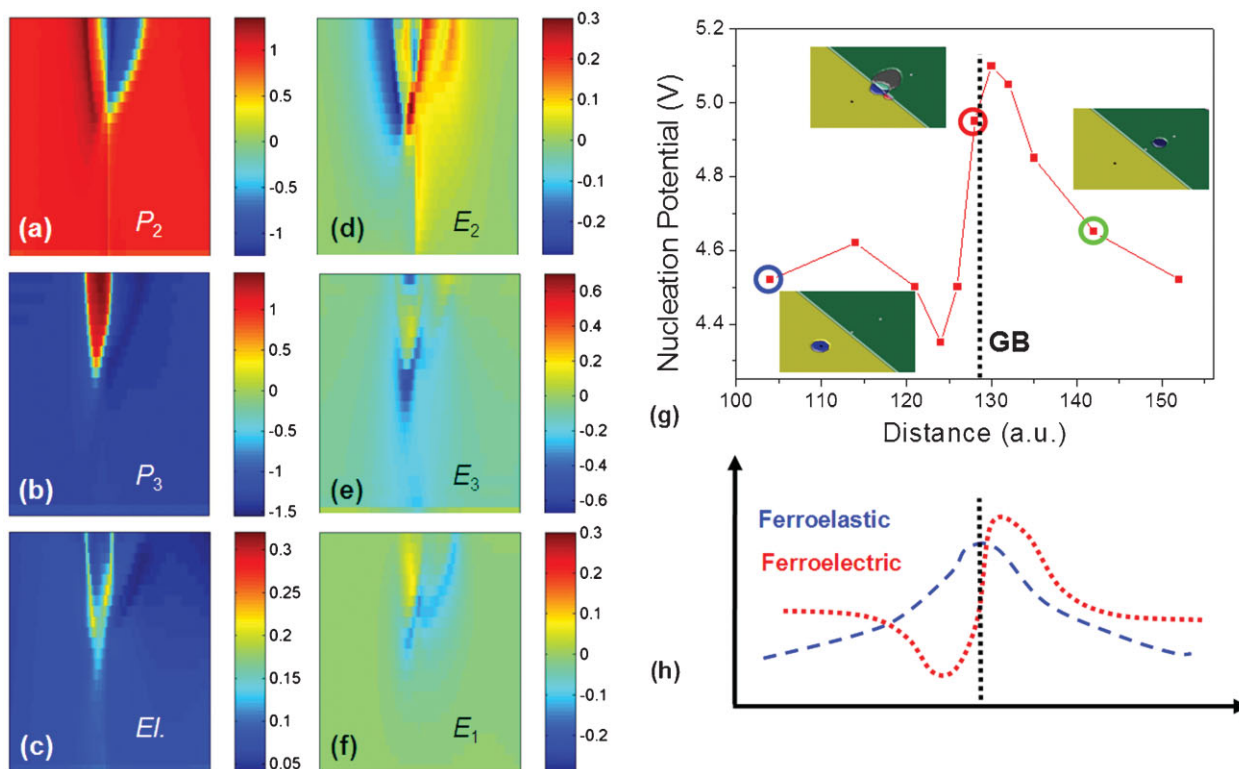


Figure 8. a) In-plane and b) vertical polarization distribution and c) corresponding elastic energy density. d) in-plane, e) vertical, and f) longitudinal electric field. g) Spatial distribution of nucleation voltage across the GB, with insets of higher resolution domain structure during nucleation of domains along the GB. The directions of polarization of the nucleated domains are indicated in the local coordinate system. h) Schematic distribution of propensity for ferroelectric and ferroelastic switching across the GB.

with proximity to the GB. Also shown is the domain structure just after nucleation for each of the tip locations. Note the characteristic evolution of nucleation potentials.

Based on these observations, we argue the GB impedes 71° polarization switching due to the built-in electric field in the near-surface region. At the same time, ferroelectric switching is facilitated at one side and impeded at the other side of the GB (Fig. 8h). Furthermore, the ferroelectric domain can serve as an efficient stabilizing center for a ferroelastic domain. The interplay between these factors yields a spectacular evolution of tip-location-dependent switching across the GB.

While the direct quantitative comparison between the experimental SS-PFM results and phase-field modeling is challenging since the relationship between domain structure and PFM signal is established only for the case of ferroelectric switching, we note the modeled behavior agrees well with experimental observations. While far from the GB hysteresis loops have an almost “ideal” shape, in the vicinity of the GB they adopt a shape demonstrating fine structure features indicative of earlier nucleation, but slower domain growth at earlier stages. Based on the modeling results, these are the signatures of the ferroelectric–ferroelastic domains. The loop shape illustrates strong variability along the GB, which is anticipated since the disorder can result in additional symmetry breaking in this direction. Finally, the nucleation potential profiles and other

relevant ferroelectric parameters exhibit a characteristic distorted S-shape, fully consistent with the phase-field modeling predictions. Thus, SS-PFM results and phase-field modeling data suggest that the GB effect on nucleation can be explained by mesoscopic electrostatic fields.

5. Conclusions

We report studies of the effect of an engineered microstructure on polarization switching in BFO using SS-PFM. Tip-induced polarization switching is reversible and allows multiple switching cycles in closely spaced locations to be measured, and thus the effects of tip-defect separation on the signal can be probed systematically. In the vicinity of the GB, the hysteresis loops are broadened, expanded in the vertical direction, and demonstrate much higher point-to-point variability compared to the regions far from the GB. In addition, the loops often exhibit fine structure indicative of defect-domain interactions.^[18] The phase-field modeling studies provide the mesoscopic picture of polarization reversal at an engineered defect and allow the mesoscopic mechanisms of switching, including GB-induced electroelastic fields, to be elucidated.^[31]

The implications of these studies are two-fold. The up-down polarization switching in (001) oriented rhombohedral BiFeO₃

can proceed along the ferroelastic and ferroelectric pathways. While the former corresponds to larger lowering of electrostatic energy, the latter leads to domain walls with smaller elastic energy densities. The choice between the two is very sensitive to the presence of inhomogeneities that break in-plane symmetry of the material. Here, this behavior was observed as the interplay between the tip field and the GB; however, similar mechanisms will be active due to electrode roughness, step edges, and other mechanisms that can give rise to lateral fields. Note that the domain nucleation process controls the kinetic pathway of the subsequent switching process. Hence, these near-surface effects can control the overall device performance.

Secondly, these studies suggest the potential of low noise, high resolution SS-PFM and associated theoretical approaches towards understanding the fundamental mechanisms for polarization reversal in ferroelectrics. While the exact atomistic picture of the switching process is yet unavailable, the combination of PFM with in situ scanning transmission electron microscopy (STEM) holds the promise for such studies. Additionally, the use of small angle GBs will ensure higher growth quality, allowing STEM studies and switching on a single defect level to be investigated, opening the pathway for the elucidation of the mesoscopic, and subsequently atomistic mechanism of phase transitions at a single defect level.

6. Experimental

Materials: Epitaxial multiferroic BiFeO₃ (200 nm) was deposited on a conductive SrRuO₃ (50 nm) bottom electrode layer on a bicrystal (0 and 24°) (001) SrTiO₃ substrate (CrysTec) by pulsed laser deposition [32].

Electron Backscatter Diffraction: EBSD was used to identify the crystallographic orientations in the material. The EBSD detector system was inside a FEI Strata 235 Dual-Beam SEM. Initially, a coarse scanning of the sample area was carried out with a beam step size of 1 μm, and diffraction patterns across the sample surface were recorded. The EBSD scans detected two specific orientations, corresponding to the two grains of the SrTiO₃ bicrystal. The grains had a common out-of-the plane (001). However, the grains were misaligned in-plane by 24°. High resolution EBSD scans are shown in the Supporting Information.

PFM and SS-PFM: A commercial scanning probe microscopy system (Veeco MultiMode NS-IIIa) equipped with additional function generators and lock-in amplifiers (DS 345 and SRS 830, Stanford Research Instruments) was used for PFM measurements. A custom-built, shielded sample holder was used to directly bias the tip. Measurements were performed using Au–Cr coated Si tips (Micromasch, spring constant $k \sim 40 \text{ N m}^{-1}$).

In PFM, the tip is brought into contact with the surface, and the local piezoelectric response is detected as the first harmonic component, $A_{1\omega}$, of the tip deflection, $A = A_0 + A_{1\omega} \cos(\omega t + \varphi)$, during application of the periodic bias $V_{\text{tip}} = V_{\text{dc}} + V_{\text{ac}} \cos(\omega t)$ to the tip. The phase of the electromechanical response of the surface, φ , yields information on the polarization direction below the tip. For c^- domains (polarization vector oriented normal to the surface and pointing downward), the application of a positive tip bias results in the expansion of the sample, and surface oscillations are in phase with the tip voltage, $\varphi = 0$. For c^+ domains, $\varphi = 180^\circ$. The piezoresponse amplitude, $A = A_{1\omega}/V_{\text{ac}}$, defines the local electromechanical activity. PFM images can be conveniently represented as $A_{1\omega} \cos(\varphi)/V_{\text{ac}}$, where $A_{1\omega}$ is the amplitude of the first harmonic of the measured response, provided that the phase signal varies by 180° between domains of opposite polarities.

In piezoresponse force spectroscopy, the dc bias offset applied to the tip is changed to follow a triangular wave, and the nucleation and growth of the

ferroelectric domain below the tip are reflected in the change of the effective electromechanical response. The resulting hysteresis loops contain information on ferroelectric switching at a single location. Spatial variability of switching behavior is probed by switching spectroscopy PFM (SS-PFM), in which hysteresis loops are acquired at each point of a user-specified grid in a manner similar to force-volume imaging in AFM or current imaging tunneling spectroscopy in scanning tunneling microscopy [33]. To conduct SS-PFM measurements, the tip approaches the surface vertically until a specified contact force is achieved (usually $\sim 500 \text{ nN}$), remains at that location during the acquisition of the hysteresis loop, is then retracted and moved to the next location in a pre-defined square-grid.

Phase-Field Modeling: The total free energy of a BiFeO₃ bicrystal thin film includes the bulk free energy F_{bulk} , domain wall energy F_{wall} , elastic energy F_{elas} , and the electrostatic energy F_{elec} , i.e.,

$$F = F_{\text{bulk}} + F_{\text{wall}} + F_{\text{elas}} + F_{\text{elec}} \quad (1)$$

The bulk free energy in a given grain is expressed in terms of polarization components using the Landau theory, i.e.,

$$F_{\text{bulk}} = \int \left\{ \alpha_1 \left[(P_1^L)^2 + (P_2^L)^2 + (P_3^L)^2 \right] + \alpha_{11} \left[(P_1^L)^4 + (P_2^L)^4 + (P_3^L)^4 \right] + \alpha_{12} \left[(P_1^L P_2^L)^2 + (P_2^L P_3^L)^2 + (P_3^L P_1^L)^2 \right] \right\} dV \quad (2)$$

where $\alpha_1, \alpha_{11}, \alpha_{12}$ are the dielectric stiffness and higher order stiffness of the bulk single crystal under stress free boundary conditions.

In order to solve the elasticity and electrostatic equations, all the tensor quantities are expressed in global coordinate system. For example, the spontaneous strain in the global system is related to that in the local system by

$$\varepsilon_{ij}^{0G} = tr_{ki} tr_{lj} \varepsilon_{kl}^{0L} \quad (3)$$

where ε_{ij}^{0L} is the stress free strain in local co-ordinate system which is related to the spontaneous polarization through the electrostrictive coefficient Q_{ijkl} as $\varepsilon_{ij}^{0L} = Q_{ijkl} P_k^L P_l^L$. Tensor tr_{ij} are the elements of the transformation matrix (TR) that relates the tensor components of property in the global co-ordinate system and those in the local co-ordinate system. For example, for a grain rotated by an angle φ about the x_3^G axis only, the transformation matrix is given by:

$$TR = \begin{pmatrix} \cos[\varphi] & \sin[\varphi] & 0 \\ -\sin[\varphi] & \cos[\varphi] & 0 \\ 0 & 0 & 1 \end{pmatrix} \quad (4)$$

The elastic energy density is given by

$$F_{\text{elas}} = \frac{1}{2} \int C_{ijkl} e_{ij}^G e_{kl}^G dV = \frac{1}{2} \int C_{ijkl} (\varepsilon_{ij}^G - \varepsilon_{ij}^{0G}) (\varepsilon_{kl}^G - \varepsilon_{kl}^{0G}) dV \quad (5)$$

where $e_{ij}^G = (\varepsilon_{ij}^G - \varepsilon_{ij}^{0G})$ is the elastic strain, ε_{ij}^G is the total strain compared to the parent paraelectric phase and C_{ijkl} is the elastic stiffness tensor. Details of the calculations of elastic energy for the film-substrate system can be obtained from Ref. [29] and references therein.

The domain wall energy is introduced through the gradients of the polarization field. For simplicity we assumed the gradient energy to be isotropic. Hence, the gradient energy density can be written as:

$$f_{\text{grad}} = \frac{1}{2} G_{11} \left[(P_{1,1}^G)^2 + (P_{1,2}^G)^2 + (P_{1,3}^G)^2 + (P_{2,1}^G)^2 + (P_{2,2}^G)^2 + (P_{2,3}^G)^2 + (P_{3,1}^G)^2 + (P_{3,2}^G)^2 + (P_{3,3}^G)^2 \right] \quad (6)$$

where G_{11} is the gradient energy coefficient and P_{ij}^G represents spatial differentiation of polarization, i.e., $P_{ij}^G = \partial P_i^G / \partial x_j^G$.

The electrostatic energy of a given polarization distribution is calculated by

$$F_{\text{elec}} = -\frac{1}{2} \int E_i^G P_i^G \quad (7)$$

where E_i^G is the i th component of the electric field. It is related to the electric displacement D_i^G through the relation, $D_i^G = \epsilon_0 \kappa_{ij} E_j^G + P_i^G$, in which, $\epsilon_0 = 8.85 \times 10^{-12}$ (Fm⁻¹) is the dielectric permittivity of the vacuum, and κ_{ij} is the relative dielectric permittivity of the ferroelectric film. If there is no space charge inside the film, the electrostatic equilibrium of the film can be obtained by solving $D_{ij}^G = 0$, where $D_{ij}^G = \partial D_i^G / \partial x_j^G$, and the summation convention for the repeated indices is employed and $i = 1, 2, 3$. As an approximation, we take into account the electric field induced by a PFM tip by solving the electrostatic equilibrium equation using a specified boundary condition,

$$\phi_{\text{substrate-film interface}} = 0, \phi_{\text{film surface}} = \phi_1(x_1^G, x_2^G) \quad (8)$$

where ϕ is the electric potential, which is related to the electric field as $E_i^G = -\phi_{,i}$. Potential $\phi_1(x_1^G, x_2^G)$ has a two-dimensional Lorentz distribution,

$$\phi_1(x_1^G, x_2^G) = \phi_0 \left[\frac{\gamma^2}{(x_1^G - x_{10}^G)^2 + (x_2^G - x_{20}^G)^2 + \gamma^2} \right] \quad (9)$$

where (x_{10}^G, x_{20}^G) is the location of the tip (the peak of distribution), γ is the scale parameter which specifies the half-width at half-maximum, and γ is set to be 10 nm in this work. The details on the calculation of electric fields are presented in Ref. [17] and references therein.

With the total free energy as a functional of the global polarization, the temporal evolution of polarization as well as domain structure is obtained by solving the time-dependent Ginzburg–Landau (TDGL) equation.

$$\frac{\partial P_i^G(\mathbf{x}^G, t)}{\partial t} = -M \frac{\delta F}{\delta P_i^G(\mathbf{x}^G, t)}, \quad i = 1, 2, 3, \quad (10)$$

where M is a kinetic coefficient related to the domain mobility and t is time.

The temporal evolution of the global polarization vector fields is obtained by solving Equation (10) numerically with the semi-implicit Fourier spectral method [34]. The domain structure is described by the spatial distribution of the local polarization components which are obtained from the global polarization components using the relation $P_i^L = \text{tr}_i P_i^G$. In the simulations, we employed a model of $256\Delta x \times 256\Delta x \times 40\Delta x$, with periodic boundary conditions along x_1^G and x_2^G axes in the film plane where Δx is the simulation grid spacing and is estimated to be 1 nm. The thickness of the film is taken as $h_f = 23\Delta x$. The substrate exerts a biaxial compressive strain of 1% on the thin film, and the gradient energy coefficients is $G_{11}/G_{110} = 0.4$ for the simulation.

Acknowledgements

The research (B. J. R., K. S., A. P. B.) performed at Oak Ridge National Laboratory's Center for Nanophase Materials Sciences was sponsored by the Scientific User Facilities Division, Office of Basic Energy Sciences, U.S. Department of Energy. The research was supported in part (S. J., S. V. K.) by the ORNL LDRD program, and in part by the U.S. Department of Energy under contracts DE-AC02-05CH11231(Y.H.C.R.R.) and DE-FG02-07ER46417(L-Q.C.). Y. H. C. also acknowledges the support of the National Science Council, R.O.C. under Contract NSC 97-3114-M-009-001 and B. J. R. acknowledges the financial support of the Alexander von Humboldt Foundation. Supporting Information is available online from Wiley InterScience or from the corresponding author.

Received: January 20, 2009
Published online: May 12, 2009

- [1] J. Scott, *Ferroelectric Memories*, Springer, Berlin **2000**.
- [2] Y. Cho, S. Hashimoto, N. Odagawa, K. Tanaka, Y. Hiranaga, *Nanotechnology* **2006**, 17, S137.
- [3] S. V. Kalinin, D. A. Bonnell, T. Alvarez, X. Lei, Z. Hu, R. Shao, J. H. Ferris, *Adv. Mater.* **2004**, 16, 795.
- [4] K. Uchino, *Ferroelectric Devices*, Marcel Dekker Inc., New York **2000**.
- [5] S. Priya, *J. Electroceram.* **2007**, 19, 167.
- [6] S. P. Alpay, I. B. Misirlioglu, V. Nagarajan, R. Ramesh, *Appl. Phys. Lett.* **2004**, 85, 2044.
- [7] V. Nagarajan, C. L. Jia, H. Kohlstedt, R. Waser, I. B. Misirlioglu, S. P. Alpay, R. Ramesh, *Appl. Phys. Lett.* **2005**, 86, 192910.
- [8] I. B. Misirlioglu, S. P. Alpay, M. Aindow, V. Nagarajan, *Appl. Phys. Lett.* **2006**, 88, 102906.
- [9] C. L. Canedy, H. Li, S. P. Alpay, L. Salamanka-Riba, A. L. Roytburd, R. Ramesh, *Appl. Phys. Lett.* **2000**, 77, 1695.
- [10] A. Yu, Emelyanov, N. A. Pertsev, *Phys. Rev. B* **2003**, 68, 214103.
- [11] M. W. Chu, I. Szafraniak, D. Hesse, M. Alexe, U. Gosele, *Phys. Rev. B* **2005**, 72, 174112.
- [12] H. P. Sun, W. Tian, X. Q. Pan, J. H. Haeni, D. G. Schlom, *Appl. Phys. Lett.* **2004**, 84, 3298.
- [13] R. F. Klie, Y. Zhao, G. Yang, Y. Zhu, *Micron* **2008**, 39, 723.
- [14] M.-W. Chu, I. Szafraniak, R. Scholz, C. Harnagea, D. Hesse, M. Alexe, U. Gösele, *Nat. Mater.* **2004**, 3, 87.
- [15] C.-L. Jia, S.-B. Mi, K. Urban, I. Vrejoiu, M. Alexe, D. Hesse, *Nat. Mater.* **2007**, 7, 57.
- [16] S. V. Kalinin, B. J. Rodriguez, S. Jesse, Y. H. Chu, T. Zhao, R. Ramesh, E. A. Eliseev, A. N. Morozovska, *Proc. Natl. Acad. Sci. U. S. A.* **2007**, 104, 20204.
- [17] S. Jesse, B. J. Rodriguez, A. P. Baddorf, I. Vrejoiu, D. Hesse, M. Alexe, E. A. Eliseev, A. N. Morozovska, J. Zhang, S. Choudhury, L. Q. Chen, S. V. Kalinin, *Nat. Mater.* **2008**, 7, 209.
- [18] S. V. Kalinin, S. Jesse, B. J. Rodriguez, Y. H. Chu, R. Ramesh, E. A. Eliseev, A. N. Morozovska, *Phys. Rev. Lett.* **2008**, 100, 155703.
- [19] A. N. Morozovska, S. V. Svechnikov, E. A. Eliseev, B. J. Rodriguez, S. Jesse, S. V. Kalinin, *Phys. Rev. B* **2008**, 78, 054101.
- [20] M. M. McGibbon, N. D. Browning, M. F. Chisholm, A. J. McGibbon, S. J. Pennycook, V. Ravikumar, V. P. Dravid, *Science* **1994**, 266, 102.
- [21] M. Kim, G. Duscher, N. D. Browning, K. Sohlberg, S. T. Pantelides, S. J. Pennycook, *Phys. Rev. Lett.* **2001**, 86, 4056.
- [22] B. J. Rodriguez, Y. H. Chu, R. Ramesh, S. V. Kalinin, *Appl. Phys. Lett.* **2008**, 93, 142901.
- [23] Figures 1 and 2 illustrate regions in which the ridge is localized at one side of GB. Figure 3 illustrates a region in which the ridge is present on both sides.
- [24] S. V. Kalinin, B. J. Rodriguez, S. Jesse, J. Shin, A. P. Baddorf, P. Gupta, H. Jain, D. B. Williams, A. Gruverman, *Microsc. Microanal.* **2006**, 12, 206.

- [25] B. J. Rodriguez, S. Jesse, M. Alexe, S. V. Kalinin, *Adv. Mater.* **2008**, *20*, 109.
- [26] B. J. Rodriguez, S. Jesse, A. P. Baddorf, T. Zhao, Y. H. Chu, R. Ramesh, E. A. Eliseev, A. N. Morozovska, S. V. Kalinin, *Nanotechnology* **2007**, *18*, 405701.
- [27] S. V. Kalinin, B. J. Rodriguez, S.-H. Kim, S.-K. Hong, A. Gruverman, E. A. Eliseev, *Appl. Phys. Lett.* **2008**, *92*, 152906.
- [28] S. Choudhury, Y. L. Li, K. E. Krill, L. Q. Chen, *Acta Mater.* **2007**, *55*, 1415.
- [29] S. Choudhury, Y. L. Li, L. Q. Chen, *Acta Mater.* **2005**, *53*, 5313.
- [30] J. X. Zhang, Y. L. Li, S. Choudhury, Y. H. Chu, F. Zavaliche, Q. X. Jia, D. G. Schlom, R. Ramesh, L. Q. Chen, *J. Appl. Phys.* **2008**, *103*, 094111.
- [31] Note that the film can contain defects not associated with the GB.
- [32] Y. H. Chu, M. P. Cruz, C. H. Yang, L. W. Martin, P. L. Yang, J. X. Zhang, K. Lee, P. Yu, L. Q. Chen, R. Ramesh, *Adv. Mater.* **2007**, *19*, 2662.
- [33] *Scanning Probe Microscopy and Spectroscopy, Theory, Techniques and Applications* (Ed: D. Bonnell), Wiley, New York **2000**.
- [34] L. Q. Chen, J. Shen, *Comput. Phys. Commun.* **1998**, *108*, 147.